Pergamon

Int. J. Heat Mass Transfer. Vol. 40, No. 18, pp. 4367–4377, 1997

Printed in Great Britain
0017–9310/97 $17.00+0.00

PII: S0017–9310(97)00063–X

Model of the transient stratified flow into a chilled-water storage tank

K. O. HOMAN and S. L. SOO

Department of Mechanical and Industrial Engineering, University of Illinois at Urbana–Champaign, Urbana, IL 61801, U.S.A.

(*Received* 8 *November* 1996 *and in final form* 7 *February* 1997)

Abstract—This paper presents numerical solutions for the flowfield transients with a single jet of cold liquid entering horizontally at the bottom of a tall tank initially filled with hotter liquid which is removed at the top of the tank. Accurate solutions of the unsteady two-dimensional Navier–Stokes and heat equations are computed for laminar flow conditions with the coupling between the flow and the temperature modeled through the Boussinesq approximation. Early in the filling process, the inflow of the higher density liquid produces a gravity current which propagates across the tank floor. When turned by the wall opposite the jet, the gravity current generates a range of internal wave phenomena which are apparent in oscillations of the thermocline. The region below the thermocline is initially filled with a complex pattern of recirculation cells, which evolves to a pattern dominated by the jet vortex as the thermocline moves away from the inlet.

1. INTRODUCTION

In the last decade, interest in chilled-water storage has increased dramatically because of its ability to shift electrical demand for space cooling from on-peak to off-peak hours. The potential benefits of this technology are significant since space cooling now represents 44% of the commercial sector's summer peak-demand for electricity [1]. With chilled-water storage, utilities achieve more uniform demand, and consumers reap savings due to the lower rates during off-peak hours. The simplest, most reliable design for chilled-water thermal storage is a single, naturally stratified tank. Although similar in principle to the storage devices commonly used in solar thermal systems, chilled-water storage tanks (1) operate with a much lower temperature difference, e.g. 10 vs 75°C, and (2) have a significantly larger storage volume, e.g. millions vs hundreds of liters. For both systems the level of mixing between the 'hot' and 'cold' liquid determines the efficiency of the storage device. The engineering objectives are to relate the storage-tank design and operation to the mixing between the hot and cold liquid, and to alter design and operation in order to optimize performance.

The earliest studies of solar thermal storage [2, 3] noted the importance of inlet design to overall performance, and a similar dependence on inlet design was identified in the early research on stratified chilled-water storage [4, 5]. Yoo *et al.* [6] focused on the first stage of the tank-filling process in which the entering cold water forms a gravity current which propagates across the tank. Yoo *et al.* [7] presented measurements of length and propagation rate for this gravity current. The relatively few numerical simulations of the tank-filling process reported in the literature [8–10] have, unfortunately, relied on schemes which are incapable of resolving the large thermal gradients observed experimentally.

In the present study, numerical methods capable of resolving the important physical scales are used to provide a quantitative description of the transient filling process. Adequate numerical resolution is believed to be of primary importance since the dynamics of the flowfield depend strongly on the temperature field, and since the level of thermal mixing is of fundamental relevance to stratified-storage performance.

2. PROBLEM FORMULATION

Our two-dimensional geometry is shown in Fig. 1. We assume that the tank is sufficiently tall that the inlet and outlet flows are decoupled. We focus on the inlet flow with appropriate outflow conditions at the top boundary. The characteristic length, velocity and time scales are chosen as the inlet height l, the area average inlet velocity $\bar{u}$, and convective time scale $l/\bar{u}$, respectively. The characteristic temperature difference, $\Delta\hat{T}$, is chosen as the difference between the initial uniform temperature in the tank and the steady inlet temperature, corresponding to the minimum and maximum density, respectively. For an unsteady, two-dimensional flow, the dimensionless vorticity, stream function and energy equations are

$$\nabla^2\psi = -\omega \tag{1a}$$

$$\frac{D\omega}{Dt} = \frac{1}{Re}\nabla^2\omega + \frac{1}{Fr^2}\frac{\partial T}{\partial x} \tag{1b}$$

NOMENCLATURE

$\hat{}$	denotes dimensional physical quantity
c	phase velocity ($\hat{c}/\bar{u}$)
d	height of gravity-current head ($\hat{d}/l$)
D	ambient fluid depth ($\hat{D}/l$)
Fr	Froude number $\hat{u}/\sqrt{g'l}$)
g, g'	gravitational constant, reduced gravity [m s^{-2}]
h	height of gravity-current nose, shallow-layer depth ($\hat{h}/l$)
H	domain height [m]
i, j	cartesian grid indices
k	wavenumber [m^{-1}]
l	inlet height [m]
n	time step index
Pr	Prandtl number (ν/α)
Re	Reynolds number ($\bar{u}l/\nu$)
Re_Δ	cell Reynolds number ($\Delta x Re/\lambda$)
t	time ($\hat{t}/(l/\bar{u})$)
T	temperature ($(\hat{T}-\hat{T}_i)/\Delta\hat{T}$)
u, v	velocity components ($\hat{u}/\bar{u}$, $\hat{v}/\bar{u}$)
$\bar{u}$	average inlet velocity [m s^{-1}]
W	domain width [m]
x, y	Cartesian coordinates ($\hat{x}/l$, $\hat{y}/l$)
y_f	fill line (t/X)
X, Y	dimensionless domain width, height (W/l, H/l).

Greek symbols

β	thermal expansion coefficient [K^{-1}]
θ	startup function as defined in equation (4)
λ	ratio of average to maximum inlet velocity
ν	kinematic viscosity [m^2 s^{-1}]
ρ	density [kg m^{-3}]
τ	period ($\hat{\tau}/(l/\bar{u})$)
ψ	stream function ($\hat{\psi}/(\bar{u}l)$)
ω	vorticity ($\hat{\omega}/(\bar{u}/l)$).

Subscripts

g	gravity current
i	inlet
m	maximum
o	startup
p	particle index.

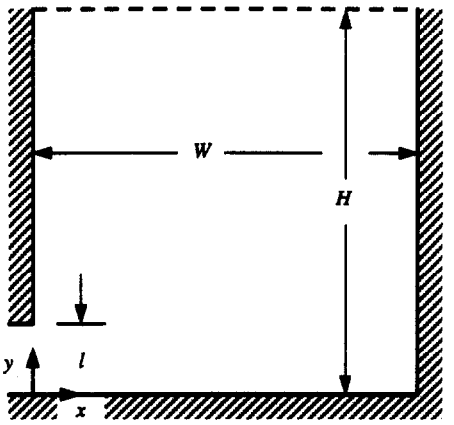

Fig. 1. Geometry and coordinate system for the lower portion of a tank with a single corner inlet.

$$\frac{DT}{Dt} = \frac{1}{Pr\,Re}\nabla^2 T \tag{1c}$$

where D/Dt denotes the substantial derivative. The domain is defined by $0 \leqslant x \leqslant X$ and $0 \leqslant y \leqslant Y$, where $X \equiv W/l$ and $Y \equiv H/l$. The Reynolds number and Froude number appearing in equations (1) are defined as $Re \equiv \bar{u}l/\nu$ and $Fr \equiv \bar{u}/\sqrt{g'l}$ where g', the reduced internal gravity, is in turn defined as $g' \equiv g(\Delta\rho/\rho) \cong g(\beta\Delta\hat{T})$. The stream function ψ, and vorticity, ω, are related to the x and y components of velocity by $u = \psi_y$, $v = -\psi_x$ and $\omega = v_x - u_y$, where the subscripts x and y denote differentiation.

The boundary conditions applied at the inlet, $x = 0$, for $0 \leqslant y \leqslant 1$, are

$$u = 6y(1-y)\,\theta(t; t_0), \tag{2a}$$

$$v = 0, \tag{2b}$$

$$T = 1 - \theta(t; t_0). \tag{2c}$$

The conditions applied along the outflow boundary, $0 < x < X$, $y = Y$, are $\psi_{yy} = 0$ and $\omega_y = 0$. Along the remaining boundaries, the conditions are

$$\psi = 0, \quad \psi_y = 0, \quad T_y = 0, \quad \text{at } y = 0, \quad 0 \leqslant x \leqslant X, \tag{3a}$$

$$\psi = 0, \quad \psi_x = 0, \quad T_x = 0, \quad \text{at } x = X, \quad 0 \leqslant y \leqslant Y, \tag{3b}$$

$$\psi = \theta(t; t_0), \quad \psi_x = 0, \quad T_x = 0, \quad \text{at } x = 0, \quad 1 \leqslant y \leqslant Y. \tag{3c}$$

The initial conditions are $\psi = \omega = 0$ and $T = 1$.

The function θ appearing in equation (2) is defined by

$$\theta(t; t_0) = \begin{cases} (t/t_0)^2(3 - 2t/t_0) & \text{for } t/t_0 \leqslant 1, \\ 1 & \text{for } t/t_0 > 1. \end{cases} \tag{4}$$

This startup function is used to ramp the inlet boundary conditions on velocity and temperature from their initial condition to their steady-state values while maintaining finite rates of change. For the results pre-

sented in this paper, the length of the startup period, t_0, has been fixed at two dimensionless time units to avoid the introduction of temporal oscillations on the convective time scale due to the numerics.

3. NUMERICAL METHOD

The governing equations are discretized on a grid with uniform spacing Δx in both coordinate directions. The points on this grid, (x_i, y_j), are given by $x_i = i\Delta x$ and $y_j = j\Delta x$. The time-stepping algorithm is based on a uniform time increment for which the time t^n is given by $t^n = n\Delta t$. The Poisson equation for the stream function, equation (1a), is discretized using central differences and is solved at each time step using a W-cycle based full multigrid correction scheme [11]. The vorticity and temperature transport equations, equations (1b) and (1c), are integrated in time using the alternating direction implicit (ADI) scheme of Briley and McDonald [12]. A Crank–Nicolson time differencing scheme is used for the diffusion operators. The advective terms are treated explicitly using the monotonic piecewise linear (MPL) scheme of van Leer [13], which is second order accurate in space. Although typically used for shock capturing, the MPL scheme has been used in the current study to capture the thin thermal interior layers without introducing the large amounts of numerical diffusion which are typical for lower-order schemes. The equations were solved sequentially in the following order: temperature, vorticity and stream function. The buoyant source term in the vorticity equation was evaluated at time level t^{n+1} since the vorticity equation was solved after the energy equation had been advanced in time.

On the inlet boundary, the value of the vorticity at time t^{n+1} was computed from the vorticity definition and the boundary condition in equation (2a). The u_y term was evaluated at time t^{n+1} using equation (2a) and the v_x term was computed at time t^n using a first-order backward spatial difference. The stream function on the inlet boundary is computed from $u = \psi_y$ and equation (2a). Along the solid wall boundaries, the vorticity value at time t^{n+1} was determined from the stream-function solution at the previous time step using equations (1a) and (3). This formula is first-order accurate in space and time. Along the outflow boundary, the zero gradient condition on vorticity was approximated using a first-order backward difference. The value of ψ^{n+1} along the upper boundary was determined by solving a discretized form of the reduced Poisson equation, $\psi^{n+1}_{xx} = \omega^{n+1}$, by direct elimination [14].

The time step, Δt, was determined by

$$\Delta t \leqslant \min\left(\lambda\Delta x, \frac{\Delta x Re_\Delta}{2}, \frac{\Delta x Re_\Delta}{Re_\Delta - 2}\right) \tag{5}$$

where Re_Δ, the cell Reynolds number, is defined as $Re_\Delta \equiv \Delta x Re/\lambda$ and the parameter λ is the ratio of the area average inlet velocity, $\bar{u}$, to the inlet velocity maximum. The explicit treatment of the advection terms in equations (1b) and (1c) leads to the first of the three terms in equation (5). This condition, $\Delta t \leqslant \lambda\Delta x$, is a form of the well-known CFL condition [15].

The spatial grid size, Δx, was determined by performing computations on a series of grids, each differing by a factor of two from the previous grid. A Richardson extrapolation based error estimate [16, 17] was used to calculate and then compare the level of resolution. During the early stages of the buoyant-inflow process, the highest error levels were located in the region where the horizontal temperature gradient, $\partial T/\partial x$, was largest. Examination of the temperature solution at $t = 8$ for example, showed that the $\Delta x = 1/8$ case had noticeably more numerical diffusion than either the case of $\Delta x = 1/16$ or $\Delta x = 1/32$. This difference was understandable when the thickness of the thermal interior layer was compared to the grid size, Δx. At $\Delta x = 1/8$, the thickness of the thermal interior layer was less than $2\Delta x$, implying that the large temperature gradient was not being resolved. For smaller Δx, the thickness of the thermal interior layer was larger than the grid size, so that resolution improved. In general, the L_2 norm of the estimated error over the entire domain was an order of magnitude smaller than any local maximum error, suggesting that the error was localized. For most of the results presented in this paper, a grid size Δx of 1/32 was used.

The outflow boundary location is not a serious concern for the present problem because the flow approaches a fully-developed profile as we move upward from the thermocline. A minimum requirement for the height of the domain would therefore appear to be $Y \geqslant t_*/X$ where t_* is the limit of the time integration interval. For the case presented in this paper, the height of the domain is $Y = 2X$ and the limit of the time integration satisfies $t_* \ll YX$.

Particle time lines—similar to the bubble time lines produced experimentally using a pulsed wire [18]—were computed as an aid in the visualization of the transient flowfield. The lagrangean position (x_p, y_p) of each massless particle was computed using

$$x_p^{n+1} = x_p^n + u_p\Delta t, \tag{6a}$$

$$y_p^{n+1} = y_p^n + v_p\Delta t \tag{6b}$$

where p is the particle index and the superscript refers to the time step. The advection velocities (u_p, v_p), are determined from a two-step Euler predictor–corrector method [19] and are evaluated at each time step using a two-variable linear-interpolation scheme [20].

4. RESULTS AND DISCUSSION

We have chosen to present results for the case in which $Re = 50$, $Fr = 1$, and $Pr = 10$. Although some full-scale systems are operated at Reynolds numbers considerably higher than 50, we have chosen this value

so that we could examine the filling process under laminar flow conditions. The choice of Froude number ensures that gravity will play a significant role in the dynamics of the filling process and the Prandtl number corresponds to that of water at approximately 10°C. The chosen geometric parameters are $X \equiv W/l = 16$ and $Y/X = 2$. As mentioned earlier, the location of the outflow boundary is intended to approximate a tank which is tall relative to the scale of the inlet.

Measured on the convective time scale, the overall filling process is a large time process. However, resolving the dynamics of the filling process on the convective time scale is crucial, since those dynamics are the source of the thermal mixing which ultimately determines the efficiency of the storage device. In the present case we will, in effect, examine only a fraction of this overall process since the focus is on the time interval necessary to fill the lower portion of a tall tank. For discussion, we have chosen to divide this filling process into three phases:

1. The initial phase in which the inflow of cold liquid forms a gravity current which propagates across the width of the tank.
2. A second phase in which internal waves are initiated by the turning of the gravity current at the wall opposite the inlet.
3. The final phase in which the jet vortex grows as the thermocline is transported away from the inlet.

This division of the filling process has been chosen because it facilitates comparison of specific characteristics of the computed flowfield with related phenomena.

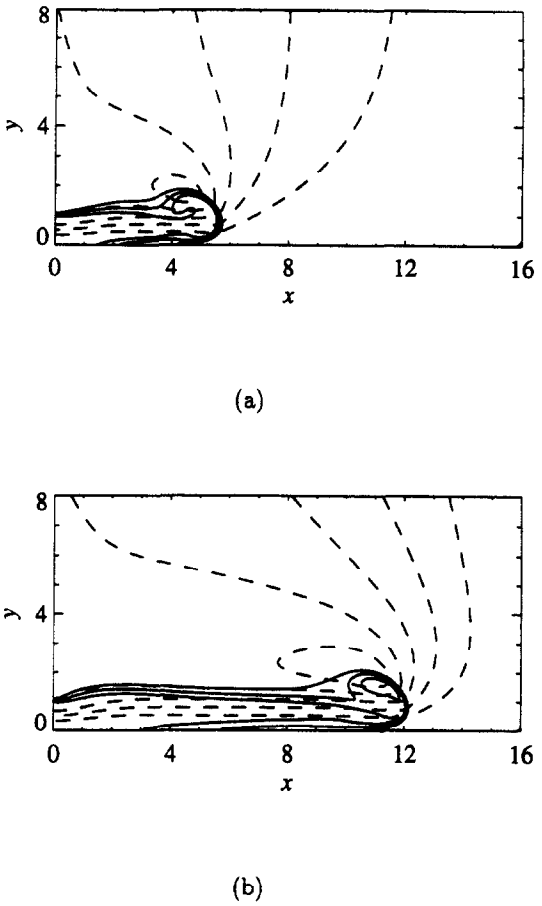

Fig. 2. Temperature contours $T = 0.1, 0.5, 0.9$ (solid lines) and instantaneous streamlines with $\Delta\psi = 0.25$ (dashed lines) for two times (a) $t = 8$ and (b) $t = 16$ during the gravity current stage.

4.1. *Gravity current*

The earliest stage of the tank-filling process occurs as cold liquid first flows across the bottom of the tank. This corresponds precisely to the definition of a gravity current as described by Simpson [21] in an extensive review of this class of buoyant-flow phenomena. Studies of gravity currents have traditionally been motivated by problems such as lock exchange and atmospheric flows. The dynamics of the present problem have much in common with these traditional applications, although certain aspects are unique to chilled-water storage tanks. Most notable of these differences is the smaller physical scale and the confined domain.

Figure 2 presents two plots of instantaneous streamlines and temperature contours for the gravity current as it propagates across the tank. We see the characteristic features of a viscous gravity current: (1) an elevated 'nose' on the leading part or 'head' of the gravity current, (2) a circulation at the rear of the head, and (3) a body of nearly uniform thickness behind the head. The recirculation cell centered on the rear edge of the gravity-current head moves with the head until it reaches the wall opposite the inlet. The separation streamline, $\psi = 1.0$, which encloses this cell originates from the upper edge of the inlet and reattaches on the wall far above the inlet. The temperature contours in Fig. 2 show that the spreading cold water flows over a thin layer of the warm fluid, which has been observed experimentally [21]. The particle time lines for a pulse-wire at $x = 8$ are shown in Fig. 3 and provide an additional view of the flowfield in the proximity of the gravity current head. At $t = 10$, the leading edge of the gravity current is located at $x \simeq 7.5$ and the time lines are in warm fluid moving forward at a velocity which is less than that of the gravity-current head. A short time later, at $t = 12$, the time lines show that the warm fluid is pushed upward after the cold-water gravity current passes the wire. The increased particle displacements are an indication of the higher velocities present in the gravity current. At $t = 16$, particles are swept forward with the leading edge of the gravity current, while other particles are swirled in the recirculating region at the rear of the gravity-current head. Finally, at $t = 20$, the time lines which have been released inside the gravity current

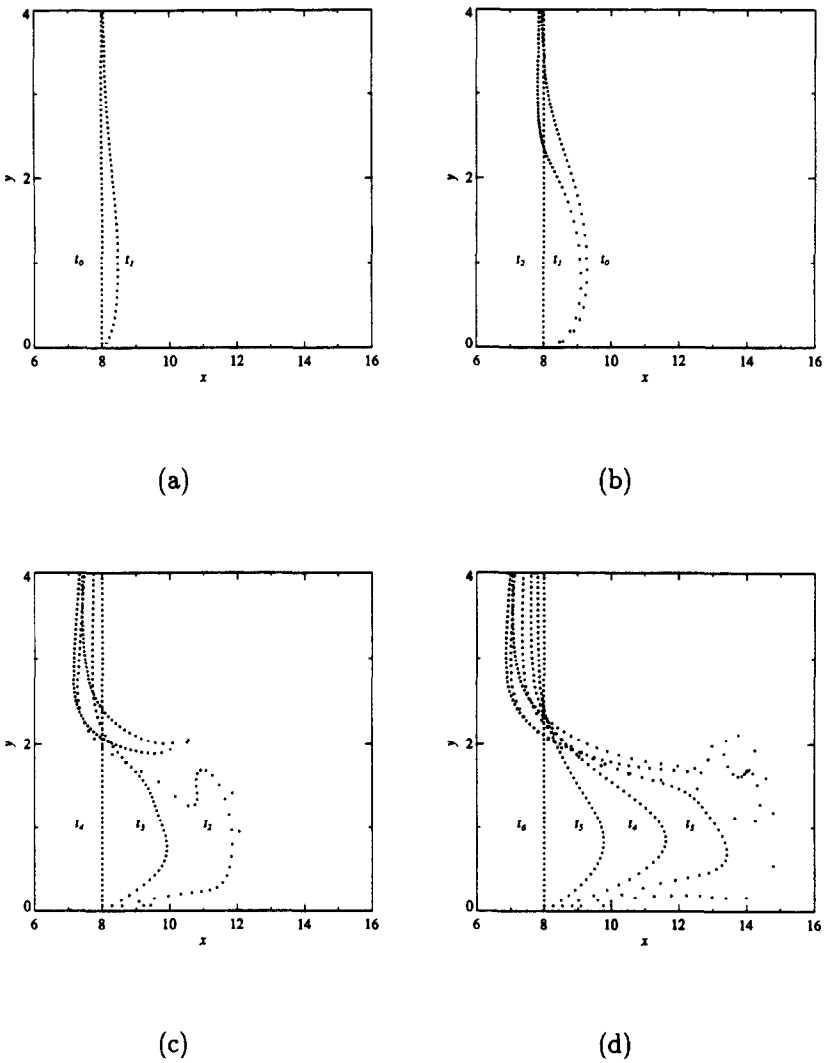

Fig. 3. Particle time lines produced by a vertical 'wire' located at $x = 8$ with a pulse interval of $\Delta t_p = 2$ shown at times (a) $t = 10$, (b) $t = 12$, (c) $t = 16$, and (d) $t = 20$.

are quite close to the time lines which would be predicted by the similarity solution for a wall jet.

The isotherms in Fig. 2 indicate that there is excellent resolution of the thermal interior layer at the leading edge of the gravity current. This resolution is a marked improvement over computational results based on schemes of first-order spatial accuracy which invariably produce unphysically large interior layers due to numerical diffusion. Experimentally, Didden and Maxworthy [22] have shown that for low Reynolds number gravity currents, the horizontal interface between the gravity-current body and the ambient fluid is rather thin; typically 10–20% of the current thickness. Similar results have also been found experimentally by Nakos [23] for gravity currents with inlet Reynolds numbers of 102 and 133. In addition, their density profiles across the gravity-current nose indicate that the scale of the horizontal temperature gradient is less than one quarter of that of the gravity-current height. Both findings compare well with the results shown in Fig. 2.

The dimensions of the computed gravity-current head were determined from the numerical results by choosing the $T = 0.9$ contour as its boundary. The location of this isotherm contour could be determined to within $\pm \Delta x/2$. The dimensionless height of the gravity-current head, d, and nose, h, are shown in Fig. 4. The gravity-current nose height is approximately 0.4 times the height of the head. This result is in agreement with the measurements of Simpson and Britter [24] who reported this ratio as varying from 0.5 to 0.15 for Reynolds numbers between 10 and 1000. The height of the gravity current head also compares favorably with their measurements. They quote the head height as varying from over 3.0 to about 0.6 for head height to ambient fluid-depth ratios of 0.05–0.3, respectively. Since, in the current problem, the simulated tank is tall and there is no ambient strati-

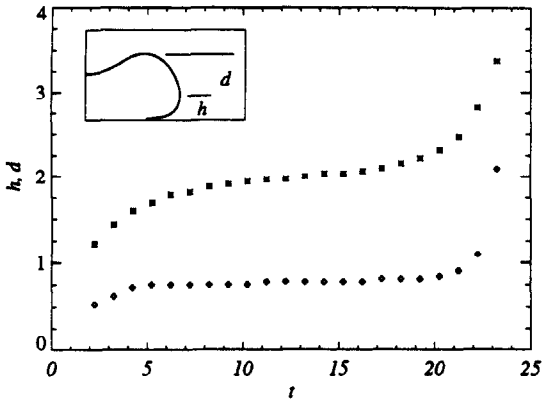

Fig. 4. The height of the gravity-current head (*) and nose (◇) as it traverses the width of the tank.

fication, the form of the gravity current is appropriate to that of a deep ambient fluid.

The velocity of the gravity current was calculated from

$$u_g \simeq \frac{x_1 - x_0}{t_1 - t_0} \tag{7}$$

where x_1 and x_0 are the position of the gravity current at times t_1 and t_0, respectively. The location of the gravity current head was again taken as the foremost point at which $T \simeq 0.9$, and could be determined to within $x = \pm \Delta x/2$. The time separation used to compute the velocity, $(t_1 - t_0)$, was 0.5. The propagation velocity is shown in Fig. 5 as a function of time. For most of the tank width, the velocity is approximately equal to 0.8. Didden and Maxworthy [22] measured the propagation rate of gravity currents for Reynolds numbers in the range from 37 to 131 and presented a correlation of the form

$$u_g = 0.73(Re/Fr^2)^{1/5}(4/5)t^{-1/5} \tag{8}$$

based on the length and time scales of the present study. At time $t = 10$, their correlation estimates the gravity current head velocity as $u_g = 0.81$. A similar correlation by Yoo *et al.* [6] developed for thermal gravity currents predicts a velocity of $u_g = 0.93$ for time $t = 10$.

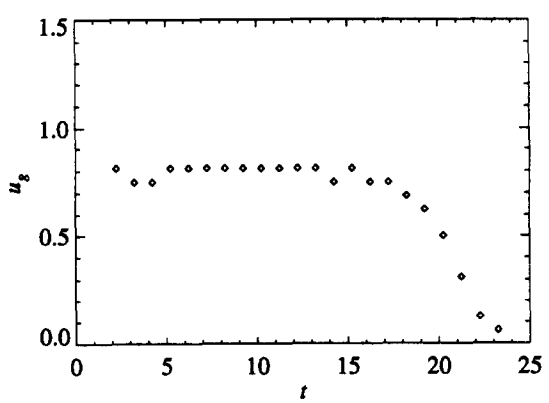

Fig. 5. The velocity of the gravity current leading edge as a function of time.

The propagation velocity is often cast in terms of a Froude number based on the propagation velocity and a characteristic height of the gravity current. The inviscid analysis of Benjamin [25] predicted

$$Fr_g = \begin{cases} 1/\sqrt{2} & \text{for } d_g/D = 1/2, \\ \sqrt{2} & \text{for } d_g/D = 0. \end{cases} \tag{9}$$

where the gravity-current Froude number, Fr_g, is based on the height of the gravity current away from the head, d_g, and D is the depth of the ambient fluid. Since, for the data shown in Fig. 5, the Froude number is equal to 1 and the gravity current depth is approximately equal to 1, the dimensionless velocity is approximately equal to the gravity current Froude number. Thus our data for u_g falls between the limits calculated by Benjamin and compares favorably to the Froude number range reported by Simpson and Britter [24] of 1.3–0.75 at d/D ratios of 0.05 to 0.3. The computational studies of Kao *et al.* [26] and Valentine and Tannous [10] predict a similar Froude number, 0.89 and 0.87, respectively, even though the horizontal temperature gradient was noticeably spread by their numerical schemes.

4.2. *Internal wave generation*

After travelling across the width of the tank, the gravity current collides with the wall at time $t \simeq 22.5$. Figure 6 presents the streamlines and temperature contours for two times shortly after the gravity current has hit the wall. At $t = 24$ the upper portion of the gravity current can be seen bouncing up the wall and turning in a counter-clockwise direction, while in the lower corner, the flow wraps in a clockwise direction. This splitting of the flow is also evident in Fig. 7(a), in which negative velocities are apparent at $x = 14$. At this time, the stagnation point on the right wall is located at $y \simeq 1.5$, while the flow below this point is turning to flow under the gravity current.

As the cold fluid bounces up along the wall, the kinetic energy of the gravity current is converted to potential energy and then back again as gravity attempts to restore equilibrium. From this sequence emerges a mixed region evident in Fig. 8(a). The temperature contours show this region very clearly, being centered at $x \simeq 11$. The stream-function contours reveal a region with instantaneously closed streamline corresponding to the lower half of this mixed region. A comparison of this figure with the horizontal velocity profiles in Fig. 7(b) shows a vortex pair-like structure centered on this mixed region with large negative velocities in the center. This region proceeds to translate across the tank while remaining vertically centered within the thermocline. This produces a noticeable thickening of the thermocline as it propagates along the thermocline. The degree of this thickening may be slightly different than observed in the flow visualization experiments of Wildin [27]; however, the

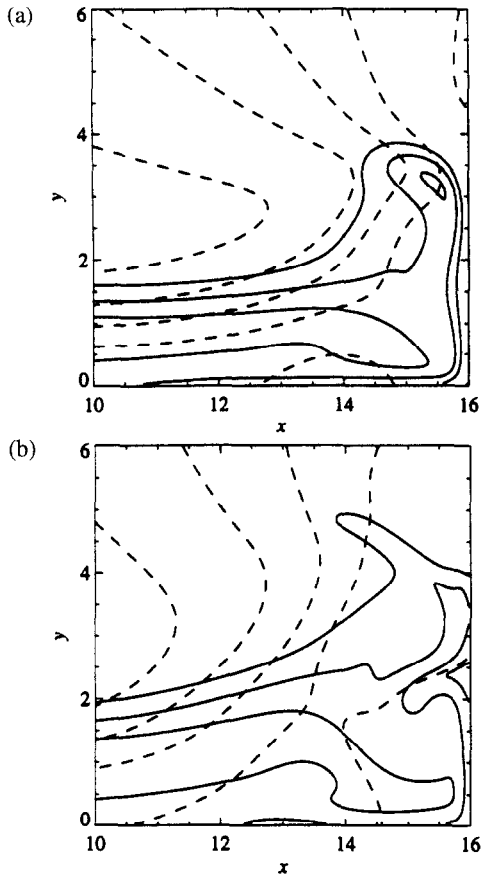

Fig. 6. Temperature contours $T = 0.1, 0.5, 0.9$ (solid lines) and instantaneous streamlines with $\Delta\psi = 0.25$ (dashed lines) for two times (a) $t = 24$ and (b) $t = 28$ during the turning of the gravity current at the wall.

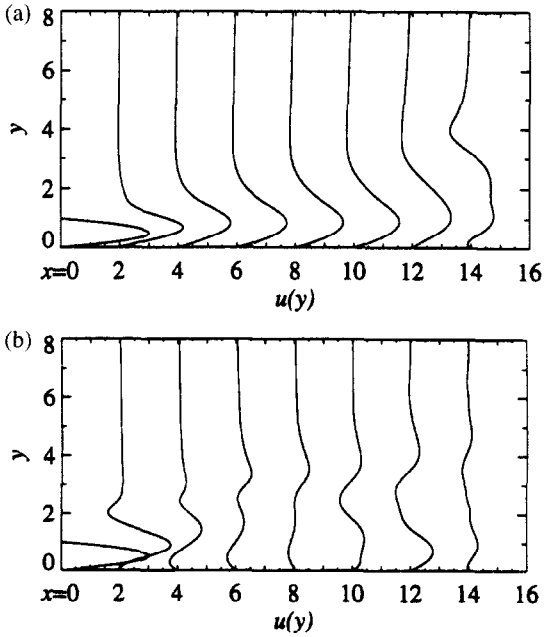

Fig. 7. Vertical profiles of horizontal velocity at times (a) $t = 24$ and (b) $t = 40$ which are during the generation and cross-tank translation of the mixed region.

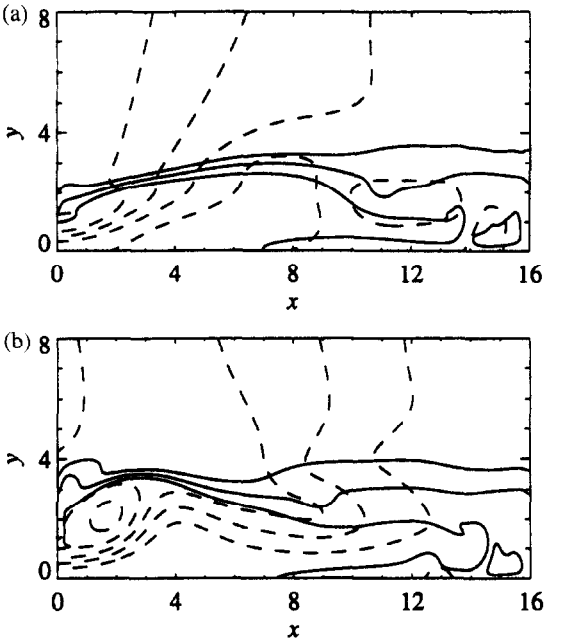

Fig. 8. Temperature contours $T = 0.1, 0.5, 0.9$ (solid lines) and instantaneous streamlines with $\Delta\psi = 0.25$ (dashed lines) for two times (a) $t = 40$ and (b) $t = 48$ during the collapse and cross-tank translation of the mixed region.

difference is quite possibly due to the small width of the present tank relative to that used in Wildin's experiments ($W/l \simeq 95$ and 155) through its influence on the turning of the gravity current at the tank wall. From Fig. 8, the propagation velocity of the mixed region is estimated to be approximately 0.3. Also of note is the deflection of the thermocline in front of the mixed region; this same structure is apparent in the flow visualization experiments of Wildin [27].

The mixed region generated by the turning of the gravity current at the right wall contains strong similarities to the methods used to produce internal solitary waves in experiments. Maxworthy [28] has stated that solitary waves are ubiquitous in thermocline-type stratification and will be produced by almost any form of mixing process. In fact, his experiments relied on the release of a fluid volume, with an excess of potential energy over the ambient, from behind a barrier to produce an initial disturbance. This disturbance evolved into a set of solitary waves as it propagated along the gradient layer. Maxworthy related the solitary waves produced in these experiments to the solitary internal waves originally examined by Benjamin [29] and Davis and Acrivos [30]. Those two studies were the first to recognize that internal solitary waves can exist in a thermocline-type stratification even if the fluid is infinitely deep both above and below the gradient layer. As described in the review by Miles [31], this occurrence of solitary waves is unique in that the scale of the disturbance is large relative to a vertical scale of the stratification rather than large relative to the fluid depth as for surface waves. The condition that the disturbance be large relative to the vertical

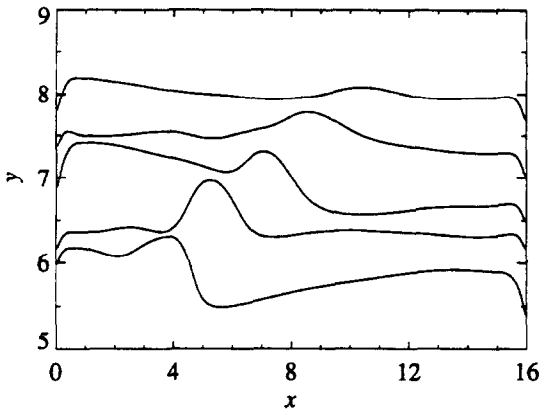

Fig. 9. Location of the 0.9 isotherm during the interval $t = 80$ to 112, in increments of 8, showing a solitary wave-like disturbance moving from left to right.

scale of the density distribution is certainly satisfied in the present case. From Fig. 6 we see that the height of the mixed region is nearly ten times the thickness of the thermocline. However, in contrast to the deep fluid analyses by Benjamin [29] and Davis and Acrivos [30], the scale of the mixed region is also large relative to the depth of one of the layers. Numerous experimental studies [32–34] have shown that quite general excitations of the gradient layer lead to solitary waves in this case as well.

The case we are considering is unique, however, in a number of additional respects compared to the experimental conditions under which internal solitary waves are typically studied. Potentially one of the more important is the relatively small width tank we have chosen to model. Most experimental studies of solitary waves are conducted in tanks which have a width many times that of the scale of the original disturbance. This provides ample time for the individual solitary waves to separate from each other, ordered by amplitude. For large initial disturbances this distance can be very large, but, in the present case, the initial disturbance is relatively small. Based on Maxworthy's data for the number of solitary waves produced vs the extent of the initial mixed region [28], the bouncing of the gravity current would almost surely produce less than three solitary waves and, more likely, only a single solitary wave. It is therefore quite plausible that the reflection of the mixed region off of the right wall is a solitary wave as illustrated by the distortion of the thermocline in Fig. 9. The speed of this solitary wave-like disturbance is approximately 0.2. This propagation velocity is smaller than the phase velocity for a linear internal wave of the same amplitude. This may be due to the fact that the horizontal scale of this region is only slightly larger than the vertical scale of the thermocline thickness, since, as noted by Kao *et al.* [35], the solitary-wave speed is decreased by a density gradient of finite thickness.

4.3. *Thermocline transport*

The thermocline begins as the interior layer separating the body of the gravity current and the ambient fluid in the tank, formed as the gravity current moves across the tank. Although thickened by the propagation of the mixed region along it, the thermocline remains intact for all subsequent time, growing in vertical extent through the action of convection and thermal diffusion.

The permanence of the thermocline is quite remarkable given its proximity to the inlet jet and the associated high velocities. Figure 10 shows the streamlines and temperature contours at two later times in the filling process, when the thermocline has moved away from the inlet. The role of the thermocline as a sort of boundary is evident upon comparison of the flowfield on either side of the thermocline. Above the thermocline, the streamlines indicate that the flow is quite uniform. The region below the thermocline is filled with a complex pattern of recirculation cells. The pattern evolves as the thermocline moves away from the inlet and the jet vortex consumes a proportionately larger fraction of the region below the thermocline. Since the height of the jet vortex is limited by the

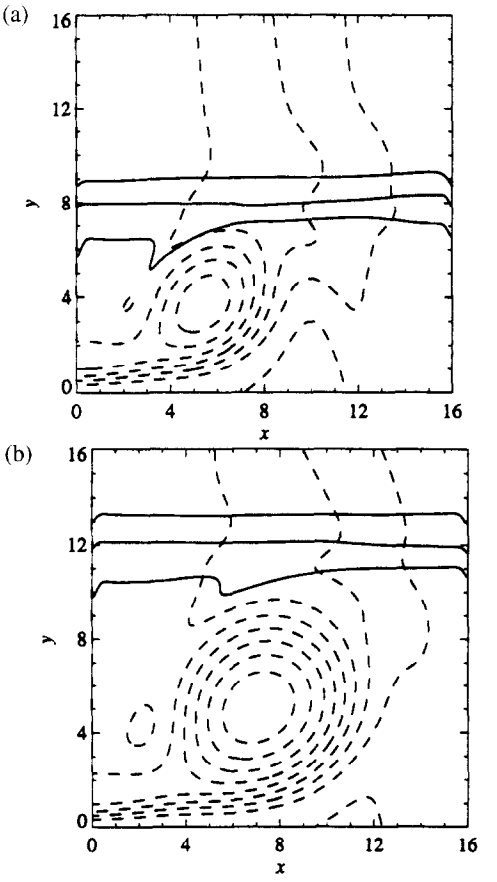

Fig. 10. Temperature contours $T = 0.1, 0.5, 0.9$ (solid lines) and instantaneous streamlines with $\Delta\psi = 0.25$ (dashed lines) for two times (a) $t = 128$ and (b) $t = 192$ showing the development of the wall jet recirculation region as the thermocline is transported away from the inlet.

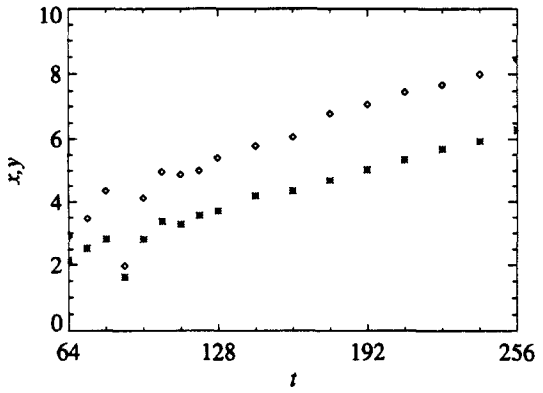

Fig. 11. Location of the stream-function maximum in time. For this time interval, the stream-function maximum is associated strictly with the jet vortex.

vertical position of the thermocline and the vortex remains essentially circular, the horizontal width too is effectively constrained by the location of the thermocline. Observation of the jet vortex in the flow visualization studies of Wildin [27] has presumably been limited by the streakline method used in the experiments. In a purely isothermal flow, which we have treated in an earlier work [36], the jet vortex fills the width of the tank at steady state, its center being located at the point $(x, y) = (7.1, 12.1)$ at time $t = 232$. This limiting behavior contrasts strongly with the movement of the stream-function maximum for the present, non-isothermal case, as shown in Fig. 11. The stream-function maximum is simply the maximum positive value of the stream function over the entire domain.

The internal waves generated by the turning of the gravity current at the right wall include not only solitary wave-like motion but also large-scale oscillations of the thermocline. Figure 12 shows time traces of temperature near each side of the tank, $x = X/8$ and $7X/8$, at the fill line, $y_f \equiv t/X$. We see a clear phase shift between the two points at opposite sides of the tank and, as also shown in Fig. 12, the horizontal velocity trace indicates a reversal of the velocity as the thermocline rocks back and forth. These oscillations are akin to the lowest-mode standing wave in basins such as lakes [37]. For this mode of oscillation, liquid sways back and forth, heaping itself up at alternating sides of the basin. The period of this oscillation is equal to the time a progressive wave would take to traverse two domain widths [38] and is given by $\hat{\tau} = 2W/\hat{c}$, where $\hat{\tau}$ is the dimensional period and $\hat{c}$ is the dimensional phase velocity. The dimensionless period of the oscillation in Fig. 12, $\tau \equiv \hat{\tau}/(l/\bar{u})$, is approximately equal to 23. This corresponds closely to a period of oscillation based on the phase velocity for a two-layer system in which the upper fluid is deep and the lower is shallow. For such a system, the phase velocity [37] is

$$\hat{c}^2 = \frac{g'}{k}(1+\coth k\hat{h})^{-1} \tag{10}$$

where $\hat{h}$ is the depth of the shallow layer, k is the wavenumber, and $\Delta\rho/\rho \ll 1$. The dimensionless phase velocity is then given by

$$c = \left[\frac{X/(\pi Fr^2)}{1+\coth \pi h/X}\right]^{1/2} \tag{11}$$

since the wavenumber k is equal to π/W for the lowest-mode standing wave. For the present case, this predicts a period of oscillation between 20 and 27 for a cold-fluid depth of 2–8.

The decay of the maximum and minimum of the horizontal velocity with increasing height, shown in Fig. 13, is exponential, as would be expected in a deep layer.

The oscillation of the thermocline has an interesting effect on the jet vortex. As seen in Fig. 12, the stream-function maximum shows an oscillation of the same period as that of the lowest mode standing wave. The explanation is that, as the thermocline moves below

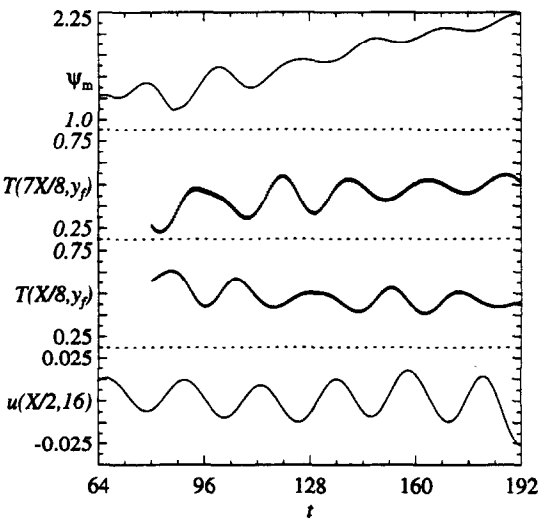

Fig. 12. Time traces of stream-function maximum, horizontal velocity and temperature showing the large scale oscillations of the thermocline.

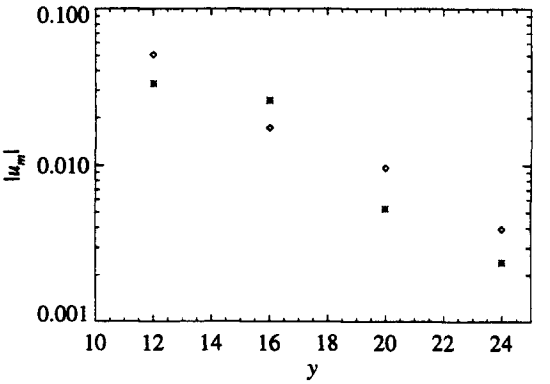

Fig. 13. Vertical decay of the horizontal velocity maximum (◇) and minimum (*) for the time interval $t = [64, 192]$.

its equilibrium level on the inlet side of the tank, the jet vortex is compressed and ψ_m decreases. Then, as the thermocline moves above the equilibrium level, the jet vortex responds by increasing its size and strength. The decreasing amplitude of the oscillations in the stream-function maximum indicate the decay of the standing-wave motion as time progresses.

5. CONCLUSIONS

The filling of a stratified-storage tank initially full of hot water by an inflow of cold water produces a wide range of gravity-driven phenomena. The initial inflow of cold fluid produces a gravity current which traverses the width of the tank, thereby forming a thermocline-type stratification. The turning of this gravity current at the wall of the tank opposite the inlet initiates a range of internal wave motions including solitary and standing waves. The presence of the thermocline forms a barrier between the uniform flow above the thermocline and the recirculating flow beneath the thermocline driven by the inlet jet.

The solitary-wave motion evident in our model of the buoyant filling process may also be the source of the motions observed by Wildin [27] and Baines *et al.* [4]. Both have observed phenomena which appear to reflect back and forth across the tank following the turning of the gravity current at the wall. In both cases, the experiments were conducted with flow parameters of the same magnitude that we have used in our model, except the tank width. In their experiments, the tank width was on the order of 100 times the inlet height, making it even more likely there would be ample sorting time for the solitary waves.

The standing-wave motion we have observed also provides a reasonable explanation for the oscillations in outlet temperature reported by Wildin [39] for a tank with a height to width ratio of less than one and a single inlet and outlet. In those experiments, the oscillations were observed at the end of the filling process for warm water flowing into the tank near its top and colder water flowing out near the bottom. As our results have shown, the large-scale oscillations of the thermocline are not rapidly damped and could potentially be detected at the outlet of a small aspect-ratio tank, such as Wildin's for filling from the bottom or top of the tank.

Acknowledgements—This research was supported by the U.S. Army Construction Engineering Research Laboratories of Champaign, IL through the AT23-EB-ESO Program. Computing time on the SGI Challenge has been provided by a grant from the National Center for Supercomputing Applications (NCSA) of Urbana, IL. The helpful discussions provided by Professors John S. Walker and Chang W. Sohn are gratefully acknowledged.

REFERENCES

1. Wendland, R. D. and Blatt, M. H., Reliable and efficient: cool storage meets the challenges of the '90s. *The Electricity Journal*, 1992, **5**, 58–63.
2. Lavan, Z. and Thompson, J., Experimental study of thermally stratified hot water storage tanks. *Solar Energy*, 1977, **19**, 519–524.
3. Loehrke, R. I., Holzer, J. C., Gari, H. N. and Sharp, M. K., Stratification enhancement in liquid thermal storage tanks. *Journal of Energy*, 1979, **3**, 129–130.
4. Baines, W. D., Martin, W. W. and Sinclair, L. A., On the design of stratified thermal storage tanks. *ASHRAE Transactions*, 1982, **88**, 426–439.
5. Wildin, M. W. and Truman, C. R., A summary of experience with stratified chilled water tanks. *ASHRAE Transactions*, 1985, **92**, 956–976.
6. Yoo, J., Wildin, M. W. and Truman, C. R., Initial formation of a thermocline in stratified thermal storage tanks. *ASHRAE Transactions*, 1986, **92**, 280–292.
7. Yoo, J., Wildin, M. W. and Truman, C. R., Traveling velocity of thermally-driven two-dimensional gravity currents. In *Natural Circulation*, ASME FED, 1987, pp. 319–324.
8. Cai, L., Stewart, Jr, W. E. and Sohn, C. W., Turbulent buoyant flows into a 2-d storage tank. *International Journal of Heat Mass Transfer*, 1993, **36**, 4247–4256.
9. Chan, A. M. C., Smereka, P. S. and Giusti, D., A numerical study of transient mixed convection flows in a thermal storage tank. *ASME Journal of Solar Energy Engineering*, 1983, **105**, 246–253.
10. Valentine, D. T. and Tannous, A. G., Stratification of a two-dimensional reservoir produced by a buoyant inflow. In *Proceedings of Symposium on Modeling Environmental Flows, ASCE/ASME Mechanics Conference*, 1985, pp. 111–117.
11. Stuben, K. and Trottenberg, U., Multigrid methods: fundamental algorithms, model problem analysis and applications. In *Lecture Notes in Mathematics*, Vol. 960. Springer, Berlin, 1982, p. 1.
12. Briley, W. R. and McDonald, H., On the structure and use of linearized block implicit schemes. *Journal of Computational Physics*, 1980, **34**, 54.
13. van Leer, Bram, Towards the ultimate conservative difference scheme. iv. a new approach to numerical convection. *Journal of Computational Physics*, 1977, **23**, 276–299.
14. Roache, P. J., Sufficiency conditions for a commonly used downstream boundary condition on stream function. *Journal of Computational Physics*, 1970, **6**, 317.
15. Anderson, D. A., Tannehill, J. C. and Pletcher, R. H., *Computational Fluid Mechanics and Heat Transfer*. Hemisphere, New York, 1984, p. 76.
16. Ferziger, J. H., Estimation and reduction of numerical error. In *Quantification of Uncertainty in Computational Fluid Dynamics*, Vol. 158 of ASME FED, 1993, p. 1.
17. Roache, P. J., A method for uniform reporting of grid refinement studies. In *Quantification of Uncertainty in Computational Fluid Dynamics*, Vol. 158 of ASME FED, 1993, p. 109.
18. Schraub, F. A., Kline, S. J., Henry, J., Runstadler, P. W. and Littel, A., Use of hydrogen bubbles for quantitative determination of time-dependent velocity fields in low-speed water flows. *ASME Journal of Basic Engineering*, 1965, **87**, 429–444.
19. Murman, E. M. and Powell, K. G., Trajectory integration in vortical flows. *AIAA Journal*, 1989, **27**, 982.
20. Roache, P. J., *Computational Fluid Dynamics*. Hermosa, Albuquerque, NM, 1976, pp. 199–201.
21. Simpson, J. E., Gravity currents in the laboratory, atmosphere, and oceans. In *Annual Review of Fluid Mechanics*, Vol. 14, Annual Reviews, Inc., 1982, pp. 213–234.
22. Didden, N. and Maxworthy, T., The viscous spreading of plane and axisymmetric gravity currents. *Journal of Fluid Mechanics*, 1982, **121**, 27–42.
23. Nakos, J. T., The prediction of velocity and temperature profiles in gravity currents for use in chilled water storage tanks. *Journal of Fluids Engineering*, 1994, **116**, 83–90.

24. Simpson, J. E. and Britter, R. E., The dynamics of the head of a gravity current advancing over a horizontal surface. *Journal of Fluid Mechanics*, 1979, **94,** 477–495.
25. Benjamin, T. B., Gravity currents and related phenomena. *Journal of Fluid Mechanics*, 1968, **31,** 209–248.
26. Kao, T. W., Park, C. and Pao, H.-P., Inflows, density currents, and fronts, *Physics of Fluids*, 1978, **21,** 1912–1922.
27. Wildin, M. W., Flow near the inlet and design parameters for stratified chilled water storage. ASME Paper No. 91-HT-27, 1991.
28. Maxworthy, T., On the formation of nonlinear internal waves from the gravitational collapse of mixed regions in two and three dimensions. *Journal of Fluid Mechanics*, 1980, **96,** 47–64.
29. Benjamin, T. B., Internal waves of permanent form in fluids of great depth. *Journal of Fluid Mechanics*, 1967, **29,** 559–592.
30. Davis, R. E. and Acrivos, A., Solitary internal waves in deep water. *Journal of Fluid Mechanics*, 1967, **29,** 593–607.
31. Miles, J. W., Solitary waves. In *Annual Review of Fluid Mechanics*, Vol. 12, Annual Reviews, Inc., 1980, pp. 11–43.
32. Kao, T. W. and Pao, H.-P., Wake collapse in the thermocline and internal solitary waves. *Journal of Fluid Mechanics*, 1979, **97,** 115–127.
33. Koop, C. G. and Butler, G., An investigation of internal solitary waves in a two-fluid system. *Journal of Fluid Mechanics*, 1981, **112,** 225–251.
34. Segur, H. and Hammack, J. L., Soliton models of long internal waves. *Journal of Fluid Mechanics*, 1982, **118,** 285–304.
35. Kao, T. W., Pan, F.-S. and Renouard, D., Internal solitons on the pycnocline: generation, propagation, and shoaling and breaking over a slope. *Journal of Fluid Mechanics*, 1985, **159,** 19–53.
36. Homan, K. O. and Soo, S. L., The steady horizontal flow of a wall jet into a tall tank of large width. *Journal of Fluids Engineering*, 1997 (in review).
37. Turner, J. S., *Buoyancy Effects in Fluids*. Cambridge University Press, Cambridge, MA, 1973, pp. 18–21.
38. Lamb, H., *Hydrodynamics*. Dover, New York, 1932, pp. 264–265.
39. Wildin, M. W., Performance of stratified vertical cylindrical thermal storage tanks, part ii: prototype tank. *ASHRAE Transactions*, 1989, **95,** 73–82.